Enabling dynamic modelling of global coastal flooding by defining storm tide hydrographs

Job C. M. Dullaart[1], Sanne Muis[1,2], Hans de Moel[1], Philip J. Ward[1], Dirk Eilander[1,2], Jeroen C. J. H. Aerts[1,2]

1. Institute for Environmental Studies (IVM), Vrije Universiteit Amsterdam, Amsterdam, The Netherlands
2. Deltares, Delft, The Netherlands

Correspondence to: Job C. M. Dullaart (job.dullaart@vu.nl)

Abstract

Coastal flooding is driven by ~~both~~ the combination of (high) tide~~s~~ and~~/or~~ storm surge, the latter being caused by strong winds and low pressure in tropical and extratropical cyclones. The combination of storm surge and the astronomical tide is defined as the storm tide. To gain understanding into the threat imposed by coastal flooding and to identify areas that are especially at risk, now and in the future, it is crucial to accurately model coastal inundation. Most models used to simulate coastal inundation at continental to global scale follow a simple planar approach, referred to as bathtub models. The main limitations of this type of models are that they implicitly assume an infinite flood duration and they do not capture relevant physical processes. In this study we develop a method to generate hydrographs called HGRAPHER, and provide a global dataset of storm tide hydrographs based on time-series of storm surges and tides derived with ~~xxx~~the global tide and surge model (GTSM) forced with the ERA5 reanalysis wind and pressure fields. These hydrographs represent the typical shape of an extreme storm tide at a certain location along the global coastline. We test the sensitivity of the HGRAPHER method with respect to two main assumptions that determine the shape of the hydrograph, namely the surge event sampling threshold and coincidence in time of the surge and tide maxima. The hydrograph dataset can be used to move away from planar to dynamic inundation modelling techniques at ~~large~~continental to global scales.

1 Introduction

Over the course of the 21st century, ~~sea level rise (SLR) will put the~~ coastal populations increasingly at risk of flooding due to sea level rise (SLR) (Oppenheimer et al., 2019). In addition, ~~as a result of increasing exposure,~~ the number of people living in coastal areas below 10 m elevation worldwide is projected to increase from over 600 million people today to more than 1 billion people by 2050 under all Shared Socioeconomic Pathways scenarios (Merkens et al., 2016), which means that the exposure will increase~~driving an increase in exposure and further increases the risk~~. Global coastal flood risk assessments ~~models~~ can ~~inform risk assessments that~~ help ~~to~~ identifying ~~which~~ areas that are potentially exposed to flooding under both current and future climate conditions (Ward et al., 2015). To setup these flood risk assessments, it is important to understand the dynamics of storm surges generated from ~~These models generally follow two steps. First, modelling the extreme water levels at the coast. Coastal flooding is generally driven by Extreme water levels are composed of tides and storm surge, and referred to as storm tides (ref). are by~~strong winds and low pressure in tropical (TCs) and extratropical cyclones (ETCs) and how these generate coastal flooding ~~, which generate a storm surge~~ (Resio and Westerink, 2008). Flood models can be used to model these coastal inundation dynamics resulting from extreme storm tides, where the storm tide is defined as the combination of

43 storm surge and the tide ~~The combination of storm surge and the tide is defined as the storm tide~~
44 (Colle et al., 2010) ~~models~~.

45 Coastal inundation models have varying levels of complexity. Global models ~~generally~~ all follow a
46 simple planar approach (Brown et al., 2018; Dullaart et al., 2021a; Kirezci et al., 2020; Lincke and
47 Hinkel, 2018; Muis et al., 2016). These models, often referred to as bathtub models, assume that any
48 land that is below a specific static water level and that is connected to the sea will be inundated. The
49 main limitation of the planar approach is that it assumes an infinite flood duration (e.g. temporal
50 evolution of a storm surge) and does not capture the physical hydrodynamic processes ~~(e.g. temporal~~
51 ~~evolution of a storm surge)~~ that drive coastal flooding. This can be partly addressed by accounting for
52 water-level attenuation (Vafeidis et al., 2019; Haer et al., 2018; Tiggeloven et al., 2020). Local to
53 regional-scale models generally apply a (hydro)dynamic modelling approach that captures the physical
54 processes that drive flooding (Lewis et al., 2013; Pasquier et al., 2019; Vousdoukas et al., 2018). Model
55 comparisons at regional scale have shown that in terms of flood extent and depth the dynamic
56 modelling approach is more accurate than the planar approach (Ramirez et al., 2016; Vousdoukas et
57 al., 2016a). Generally, the planar approach overestimates the flood extent due to the assumption that
58 flood propagation is only limited by topography, and that high water levels are maintained for an
59 infinite duration (Stephens et al., 2021). The main reasons for applying the planar approach at the
60 continental to global scale, instead of the dynamic approach, are the simplicity of setting up a planar
61 model, low computational costs, and limited requirements for input data.

62 Due to the advances in high-performance computing and the development of reduced-physics
63 dynamic inundation models (Leijnse et al., 2021; Yin et al., 2016; Bates et al., 2010), there is the
64 potential to improve continental- to global-scale flood mapping and step away from using the planar
65 approaches for ~~global~~ large-scale coastal inundation modelling. First applications of dynamic
66 inundation models at continental scale have been published (e.g. Vousdoukas et al., 2016a). However,
67 ~~global~~ flood maps are often derived for a specific return period (RP), for example a flood map
68 corresponding to the 1 in 100-year water level. While planar models only need information about the
69 height of the extreme water level, dynamic models also need information about the duration. The
70 temporal evolution of an extreme water level, composed of tide and surge, is referred to as the
71 hydrograph (Chbab, 2015; Sebastian et al., 2014; Salisbury and Hagen, 2007). Throughout this study
72 we use the term hydrograph to refer to the storm tide hydrograph. Hydrograph characteristics that
73 determine the flood severity are, among others, the maximum storm tide level, base duration, and
74 overall shape. For example, when the water level is elevated for a longer period of time, particularly
75 close to the time of high water when defence exceedance is most likely, the water will propagate
76 further inland (Santamaria-Aguilar et al., 2017; Quinn et al., 2014). Currently, a global dataset of
77 hydrographs that can be applied for dynamic inundation modelling for specific RPs is lacking.
78 Vousdoukas et al. (2016) made a first step towards dynamic inundation modelling at the continental-
79 scale for Europe. In this study, the temporal evolution of extreme water levels is incorporated by the
80 use of a generic empirical formulation. The surge hydrograph is assumed to be an isosceles triangle
81 with a duration based on a linear fit relationship between modelled surge heights and the half event
82 duration. In reality the rising and falling limb of the surge hydrograph can have a distinct shape that
83 have different durations, and varies from location to location (MacPherson et al., 2019). The tidal
84 component in Vousdoukas et al., (2016) is represented by taking the highest tidal level from a 10-year
85 ~~period~~ simulation. Instead, a time-varying value could be used to include tidal variation, including the
86 spring-neap cycle, in a more accurate way. While some advances have been made in modelling storm
87 tide hydrographs, the current understanding of the temporal evolution of sea levels during extremes
88 is limited.

89   The aim of this study is to address this research gap by developing and applying a globally-applicable
90   method (HGRAPHER) to generate hydrographs. In doing so, we pave the way for continental to global-
91   scale coastal flood mapping using dynamic models. First, we review the various methods available to
92   define a hydrograph and their main assumptions. Second, building on the existing literature, we
93   present the new open-source HGRAPHER method with a global dataset of hydrographs for 23,226
94   locations along the world's coastline. As input, we use 38 years of storm surge and tide simulations
95   (1979-2018) from derived with the Global Tide and Surge Model (GTSM) forced with the ERA5 climate
96   reanalysis (Muis et al., 2020). Third, the sensitivity of the HGRAPHER method is tested with respect to
97   two main assumptions that determine the shape of the hydrograph, namely: 1) using normal high tide
98   or spring tide; and 2) the coincidence of the surge and tide maximum or a time offset between the
99   two maximums. Last, we discuss the limitations of our methodology and ways forward.

2 Available methods to generate hydrographs

100

101 In this section we give an overview of four hydrograph generating methods. The reason for including
102 these studies on hydrographs in this review, from the wide variety of studies that exists on this topic
103 (e.g. Sebastian et al., 2014; Chbab, 2015; Environment Agency, 2018; MacPherson et al., 2019;
104 Vousdoukas et al., 2016a; Xu and Huang, 2014; Salisbury and Hagen, 2007), is that they all have a
105 clearly distinct methodology. Based on this review, we can select the hydrograph generating method
106 that best fits our study goals. All four methods use multi-year water level time series from tide gauge
107 stations or model simulations as input, but they differ in terms of input parameter used, the way the
108 surge hydrograph is computed, and how tide and surge levels are combined. Table 1 summarizes the
109 main characteristics of the four methods.

110 **Table 1:** Main characteristics of four hydrograph methods

study	study area	hydrograph method		
		input parameter	surge hydrograph	combine tide and surge
Chbab, 2015	Dutch coast	surge residual	averaging	linearly
Environment Agency, 2018	United Kingdom coast	skew surge	fit distribution	joint probability method
MacPherson et al., 2019	German Baltic Sea coast	storm tide	parametric	not required
Vousdoukas et al., 2016	European coast	surge and wave setup	best linear fit relationship	constant value for tide

111

112 The first method by Chbab (2015) starts by computing the residual water level. The surge residual is
113 the difference between the predicted tide and the storm tide level (*Fig. 1*). Predicted tides are
114 estimated by harmonic analyses to determine the amplitude and phase of the different tidal
115 constituents. To define the surge hydrograph, events are selected from the residual time series by
116 means of the Peaks-Over-Threshold (POT) method using 0̶1.5 m as a threshold. A̶The 36̶48-hour period̶
117 time window lasting from 24 hours before until 24 hours and̶ after the surge maximum is extracted.
118 The final step to obtain the surge hydrograph is normalizing and averaging all 7̶2̶48-hour time series
119 of surge levels. To test the sensitivity of the surge hydrograph to the chosen parameters, a sensitivity
120 analysis is performed. They conclude that the upper 50% of the normalized surge height (normalized
121 surge height > 0.5) is not affected when either the threshold or time window length is increased or
122 decreased. This is an important finding because it indicates that the surge hydrograph is most robust
123 close to the time of high water when defence exceedance is most likely (Santamaria-Aguilar et al.,
124 2017; Quinn et al., 2014). However, a longer time window (of e.g. 72 or 96 hours) results in a longer
125 base duration. The argument given for using a 48-hour time window is that 48 hours is the typical
126 duration of a storm along the Dutch coastline. The surge hydrograph is added linearly to the average
127 tidal cycle where the surge maximum is assumed to coincide with the tide maximum. To generate a
128 hydrograph corresponding to a specific RP, the unitless surge hydrograph is scaled to a certain water
129 level. For example, if the average maximum tide is 1 metre and the 100-year storm tide is 3 metres,
130 the surge hydrograph is multiplied by 2. In areas with a large tidal range and a wide and shallow
131 continental shelf, tide-surge interaction may induce a time offset between the two maxima (*Fig. 1*).
132 For example, in the North Sea the surge maximum generally occurs 2.5 hours before the tidal
133 maximum (Chbab, 2015; Horsburgh and Wilson, 2007). This is because a storm surge increases the
134 depth and thereby modulates the influence of bottom friction and the speed of the tidal wave (Pugh,
135 1996; Rego and Li, 2010). The time offset can be taken into account by computing the time offset
136 between the surge and tidal maxima for all surge events above the POT 99th percentile (POT99).
137 Subsequently, the average offset is used to shift the surge time series relative to the tidal maximum.
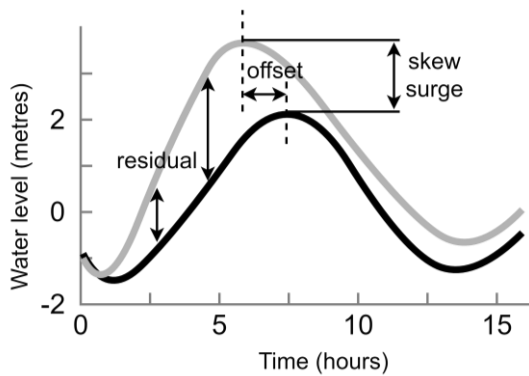
138

Figure 1: schematic of the residual, offset, and skew surge. Time series of the tide (grey line), and the tide including meteorological effects (black line) are shown.

139 The second method, developed by the U.K. Environment Agency (2018) starts by computing the skew
140 surge. Skew surge (*Fig. 1*) refers to the difference between the maximum storm tide level and
141 maximum tidal level within a tidal cycle, irrespective of their timing (Williams et al., 2016). An
142 important reason for using skew surge instead of the surge residual is that the latter can arise due to
143 tide-surge interaction (Idier et al., 2019). In contrast to the surge residual, for the skew surge there is
144 no need to account for timing offsets, apart from some locations where a dependency between skew
145 surge and high tidal levels is observed (Santamaria-Aguilar and Vafeidis, 2018). To generate the skew
146 surge hydrograph, the 15 most extreme skew surges are selected. An argument for selecting this
147 number of events is not given. Both the high and low water skew surge values are extracted for each
148 storm event. Subsequently, the high and low water skew surge values are interpolated to a 15-minute
149 timeseries and normalized. Then, the duration of each of the 15 surges at particular percentiles (i.e.
150 10%, 20% and so on) are calculated. The maximum duration at each percentile is used to compute the
151 skew surge hydrograph. The study by U.K. Environment Agency does not combine the skew surge
152 hydrograph with tidal level time series.

153 The third method by MacPherson et al. (2019), that further developed the method from (Wahl et al.,
154 (2011, 2012), starts by identifying storm tide events. To do this, a POT method is used. Using POT is
155 preferred over annual maxima because the number of events extracted is typically higher with POT
156 resulting in a more robust representation of the local storm tide characteristics in the hydrograph.
157 Then, each event is characterized through a parameterization scheme. A total of 17 parameters are
158 calculated such as peak water level, event duration, and the flow (rising limb) and ebb (falling limb)
159 curve shape. Subsequently, synthetic hydrographs are generated through Monte Carlo simulations
160 using the obtained parameters. This means that for a single return period multiple storm tide
161 hydrographs are available with different shapes but the same maximum water level.

162 The fourth method by Vousdoukas et al. (2016) starts by computing the high tide water level (HTWL).
163 The HTWL is calculated as a constant water level that consists of the mean sea level (MSL) and the
164 maximum tide elevation taken from a 10-year time series. The assumption that the maximum high
165 tidal level occurs along the entire duration of the event, thereby neglecting tidal variations, can
166 significantly overestimate the water level in places with large tidal variability, such as north-western
167 Australia. The HTWL is then combined with time-varying storm surge levels and wave setup to obtain
168 total water levels. Time series of storm surge levels (1979-2014) are taken from Vousdoukas et al.
169 (2016b) and wave setup is approximated by 20% of the significant wave height, both based on the
170 ERA-Interim global climate reanalysis (Dee et al., 2011). To obtain information about the temporal
171 evolution of an extreme event, extreme events are identified in the available time series of surge and

172   wave setup. For each identified event the duration and peak water level are extracted. Subsequently,
173   a best linear fit relationship between the duration and peak water level is estimated. To conclude, the
174   combined hydrograph consists of the HTWL combined with a symmetric triangle shaped time series
175   on top of it representing the surge and wave setup for a certain return period.

176   Comparing the four methods, we find that the hydrograph generating methods that are developed for
177   application at smaller scales are tailored towards the local water level characteristics. This makes them
178   less suitable for application at larger scales. For example, in the study by Chbab (2015) a threshold of
179   0.5 m is used to identify extreme surge events in time series. However, at the global scale surge levels
180   exceeding 0.5 m do not occur in some regions such as the south of the Caribbean. The hydrograph
181   generating method developed by U.K. Environment Agency (2018) is developed for regions that
182   experience a substantial tidal range such as the U.K., as it is based on skew surge values. However, the
183   complete global coastline does not experience such high tides. In addition, MacPherson et al., (2019)
184   developed a method that is applicable in areas with a small tidal range, making it well suited for the
185   German Baltic Sea coast and larger scales such as the entire Baltic Sea, but inapplicable at ~~larger~~
186   ~~scales~~continental to global scales. The last study that we discussed (Vousdoukas et al., 2016a) takes a
187   more simple approach to define hydrographs for continental Europe. The tidal component is
188   represented by a constant value and is combined with a triangle shaped time-varying storm surge.
189   Overall, the study by Vousdoukas et al. (2016a) is a step towards modelling inundation at larger scales
190   using hydrographs. However, substantial improvements can be made to the hydrograph generating
191   method. To this end, we will build on Chbab (2015) because, most importantly, the method used in
192   this study does take a time-varying surge and tide component into account. In addition, instead of
193   representing the surge by a triangle shape in the combined hydrograph like Vousdoukas et al. (2016a),
194   the method from Chbab (2015) allows the rising and falling limb of the hydrograph to have different
195   shapes. This results in a more accurate representation of the shape of the storm surge in the combined
196   hydrograph. It is especially important that the hydrograph represents the water level correctly close
197   to high water when defence exceedance is most likely, and because the water will propagate further
198   inland if the water level is elevated for a longer period of time (Santamaria-Aguilar et al., 2017; Quinn
199   et al., 2014).

3 Methods

Figure 1 summarizes the main steps of the HGRAPHER hydrograph generating model. Storm tide levels, tidal time series, and storm tide RPs are used as input. First, extreme events are identified in the surge time series and used to compute a normalized surge hydrograph. Second, the average tide signal is computed from the tidal time series, Third, the hydrograph is generated by combining the average tide signal with the normalized surge hydrograph. To create the final hydrograph, this generic shape is scaled to an absolute water level height for specific RPs based on the COAST-RP dataset (Dullaart et al., 2021b).

3.1 Input data
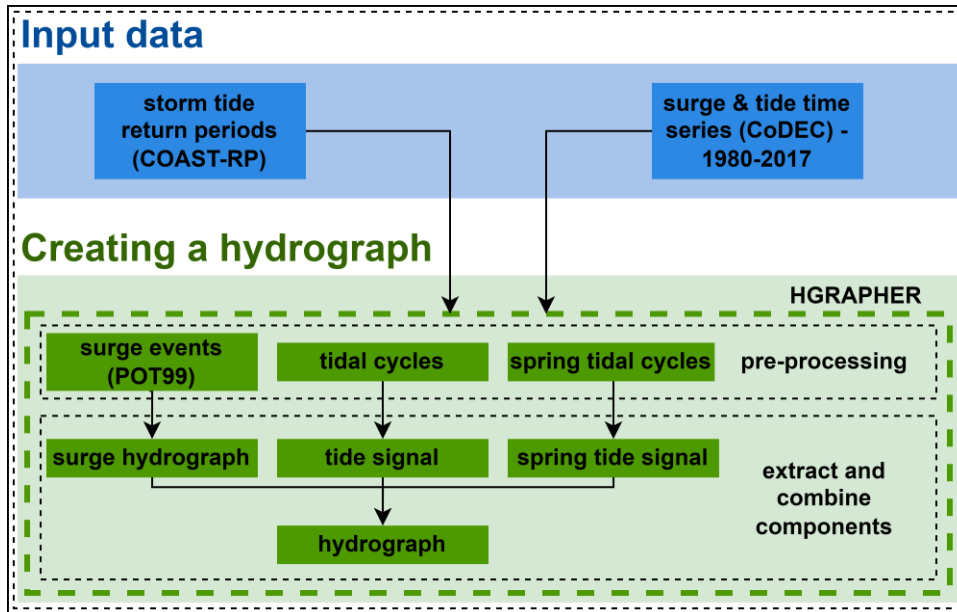
Figure 2: Modelling framework

Time series of storm tides (1980-2017) at a 10-minute interval from 23,226 output locations are taken from the CoDEC-ERA5 dataset (Muis et al., 2020). The CoDEC-ERA5 dataset was generated by forcing the 2D depth-averaged hydrodynamic Global Tide and Surge Model (GTSM) with wind and pressure fields from the ERA5 climate reanalysis (Hersbach et al., 2019). GTSM forced with ERA5 has shown to accurately simulate maximum surge heights of historical TC and ETC events (Dullaart et al., 2020). In addition, a comparison between modelled and observed annual maxima, showed a mean bias of -0.04 m (with a standard deviation of 0.32 m) (Muis et al., 2020). Overall, the time series of surge and tidal levels from the CoDEC-ERA5 dataset are of good quality and therefore valid input data to HGRAPHER. The surge time series are computed as the difference between a storm tide simulation and a tide-only simulation. As a result, the surge time series include non-linear tide-surge interaction effects (Horsburgh and Wilson, 2007). The output locations are located at every 50 km along the coastline. In addition, the locations of tide gauge stations are included. In order to scale the hydrograph to a storm tide level that corresponds with a certain RP, we use storm tide RPs from the global COAST-RP dataset (Dullaart et al., 2021b). In contrast to other global storm tide RP datasets, COAST-RP explicitly takes into account low-probability high impact TCs (Dullaart et al., 2021a) by making use of 3,000 years of synthetic TC tracks from the STORM dataset (Bloemendaal et al., 2019).

3.2 Creating a hydrograph

3.2.1 Surge hydrograph

The following procedure is used for each of the 23,226 output locations individually. To generate a hydrograph of the surge, we start with extracting independent extremes from the surge time series based on the Peaks-Over-Threshold (POT) method. Using the POT method for selecting extremes is preferred over annual maxima as the latter could result in excluding extreme events that happened in the same year. We use the 99th percentile over the complete time series as threshold and we select peaks that are at least 72 hours apart to ensure independent events (Wahl et al., 2017; Vousdoukas et al., 2016b; Haigh et al., 2016). The threshold results in the selection of on average 1 surge event per year and 40 events over the full time series. Setting the threshold is a trade-off between having an event set of sufficient size to compute a representative average shape without including too many relatively small surge events that would too strongly affect the resulting shape (see section 4.4). For each selected surge event, we first extract the time series from 36 hours before, until 36 hours after the peak (*Fig. 3a*). Second, each 72-hour surge event is normalized (i.e. dividing each surge level by the peak) such that the maximum surge value is equal to 1 (unitless). Third, we combine the selected surge events to calculate the average surge hydrograph. This is done by determining the time (relative to the peak) at which a specific surge height (from 0 to 1 with increments of 0.01) is exceeded. As an example, in Fig. 3a we show that for one surge event the exceedance time at a normalized surge height of 0.25 is 14.0 hours before and 26.0 hours (16.0 + 10.0) after the surge maximum occurred as indicated by the black arrows. Then, for each normalized surge height the average exceedance time is computed, similar to Chbab (2015), resulting in an average curve. Because the shape of the rising and falling limb of the surge can differ, the exceedance time is calculated separately for each, and they are subsequently merged into the final average surge hydrograph.

3.2.2 Average and spring tide signal
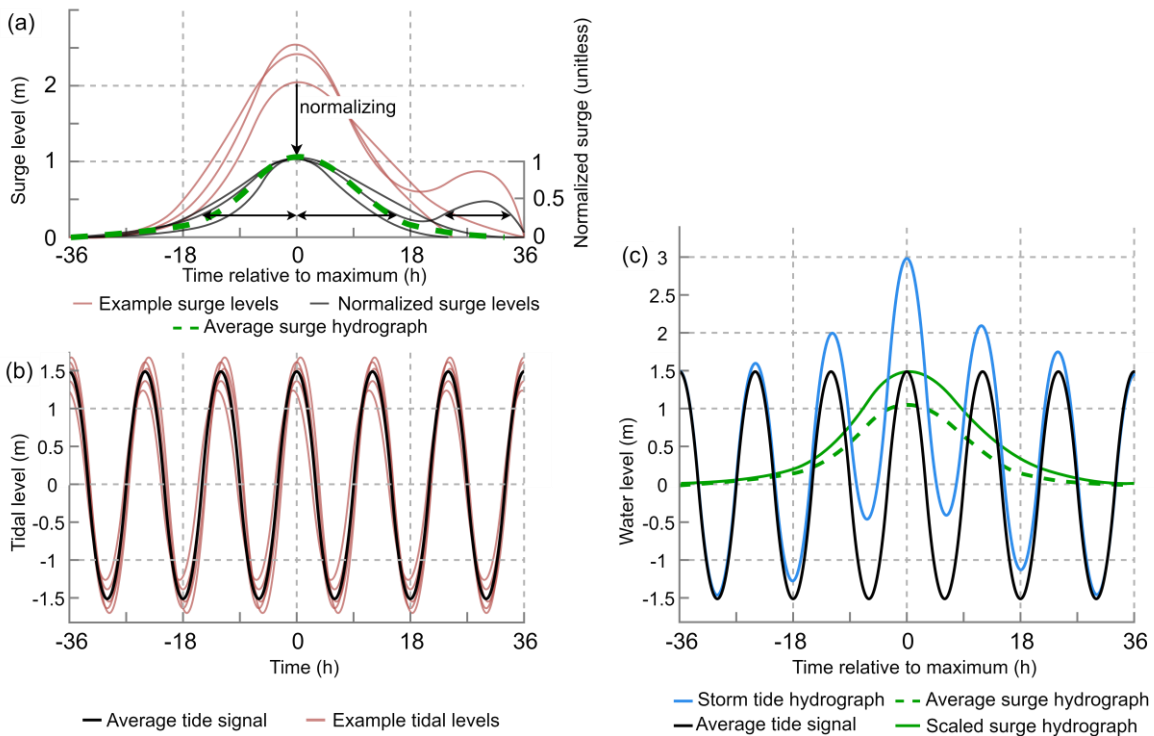
Figure 3: Visualization of the steps leading to the storm tide hydrograph of a hypothetical 1-in-100 year event of 3.0 m with the a) surge hydrograph, where the black arrows indicates the period over which a normalized surge height of 0.25 is exceeded. Note that for the falling limb we take the sum of the two time periods for which this is the case; b) average tide signal, and c) storm tide hydrograph. The average surge hydrograph is scaled to 1.5 m such that the combined water level equals the 1-in-100 year storm tide level of 3.0 m.

250 Next, we combine the surge hydrograph with the average tide signal (*Fig. 3b*). To create a curve
251 representing the average tide signal we take three steps. First, we split the tidal series from the period
252 1980-2017 up into segments that are each 24 hours and 50 minutes long. ~~we extract all tidal cycles of~~
253 ~~24 hours and 50 minutes from the period 1980-2017.~~ The start and end times of the tidal cycles are
254 selected from the tide time series by searching for a minimum around 24h and 50 minutes after the
255 previous low tide. The segment length is based on the phase of the M2 tidal component which is equal
256 to a lunar day (24 hours and 50 minutes). At most locations around the world the M2 is the main tidal
257 component. Second~~Last~~, we compute the mean over all tidal ~~cycles~~ segments to ~~extract~~ obtain the
258 average tide ~~signal~~segment. Third, we duplicate the average tide segment to obtain a longer tidal time
259 series to which we refer as the average tide signal.

260 In addition, we extract the spring tide signal because a storm surge event happening at spring tide can
261 result in a very different shape of the hydrograph. The spring-neap tide cycle takes two weeks. To
262 extract the average spring tide signal, we first search for the highest tide every two weeks. Second,
263 we select 72 hours of the tidal time series before and after the spring tide maximum. This procedure
264 is repeated for the available time series of the tide (1980-2017), after which we compute the mean
265 over all spring tides to extract the average spring tide signal.

266 3.2.3 Storm tide hydrograph
267 The surge hydrograph is combined with the average tide or spring tide to create a storm tide
268 hydrograph (*Fig. 3c*). In theory the surge maximum can coincide with any tide. However, in shallow
269 regions the timing will be influenced by interaction effects between the surge and the tide which
270 results in a phase difference. This is for example the case in the North Sea where the tidal wave will
271 start travelling faster under storm conditions due to the increased water level which reduces the
272 bottom friction (Horsburgh and Wilson, 2007; Resio and Westerink, 2008). To determine whether a
273 typical time offset between the surge and tide should be taken into account, we extract the
274 distribution of the timing offset between the surge and tidal maximum during the most extreme surge
275 events (POT99). For most locations around the globe, the distribution of the timing offset does not
276 show a clear signal (see section 4.4). Therefore, we assume that the surge and tidal maximum coincide.
277 With HGRAPHER a hydrograph can be generated for a total water level of interest. In this study we
278 use storm tide levels corresponding to a 100-year return period (RP100) because this is an often-used
279 coastal protection standard (Lamb et al., 2018; FEMA, 1968). If, for example, the RP100 storm tide
280 level is 3.0 meters and the average high tide is 1.5 meter this means the unitless average surge
281 hydrograph has to be scaled up to 1.5 meters, such that maximum surge plus the maximum tide is
282 equal to 3.0 meters (*Fig. 3c*).

4 Results

4.1 Storm surge hydrographs

For each output location from the CoDEC-ERA5 dataset, a surge hydrograph is generated. For illustration, results are shown for La Rochelle in France and Marco Island in the United States (*Fig. 4a & 4b*). We find a storm surge duration (i.e. the time over which the normalized surge height is above zero) of 54 hours in La Rochelle and 42 hours in Marco Island. Other studies find comparable storm surge durations of 40 hours for Hoek van Holland and 45 hours for Den Helder in The Netherlands (Chbab, 2015), and between 40 and 70 hours for the German Baltic Sea coast (MacPherson et al., 2019). The difference in storm surge duration between La Rochelle and Marco Island is likely caused by the different type of storms occurring in these regions. TCs can cause a fast shift from onshore to offshore winds when making landfall, which results in the surge becoming negative in just a couple of hours. Hurricane Irma is an example of a TC that made landfall near Marco Island and caused such a fast shift in surge levels. The normalized surge level time series have a strong irregular behaviour. This originates from the fact that the surge time series are obtained by subtracting tide-only simulations from a total water level simulations (including tidal and meteorological forcing). Therefore, the surge time series are the residual water level that include tide-surge interaction effects, and we believe this
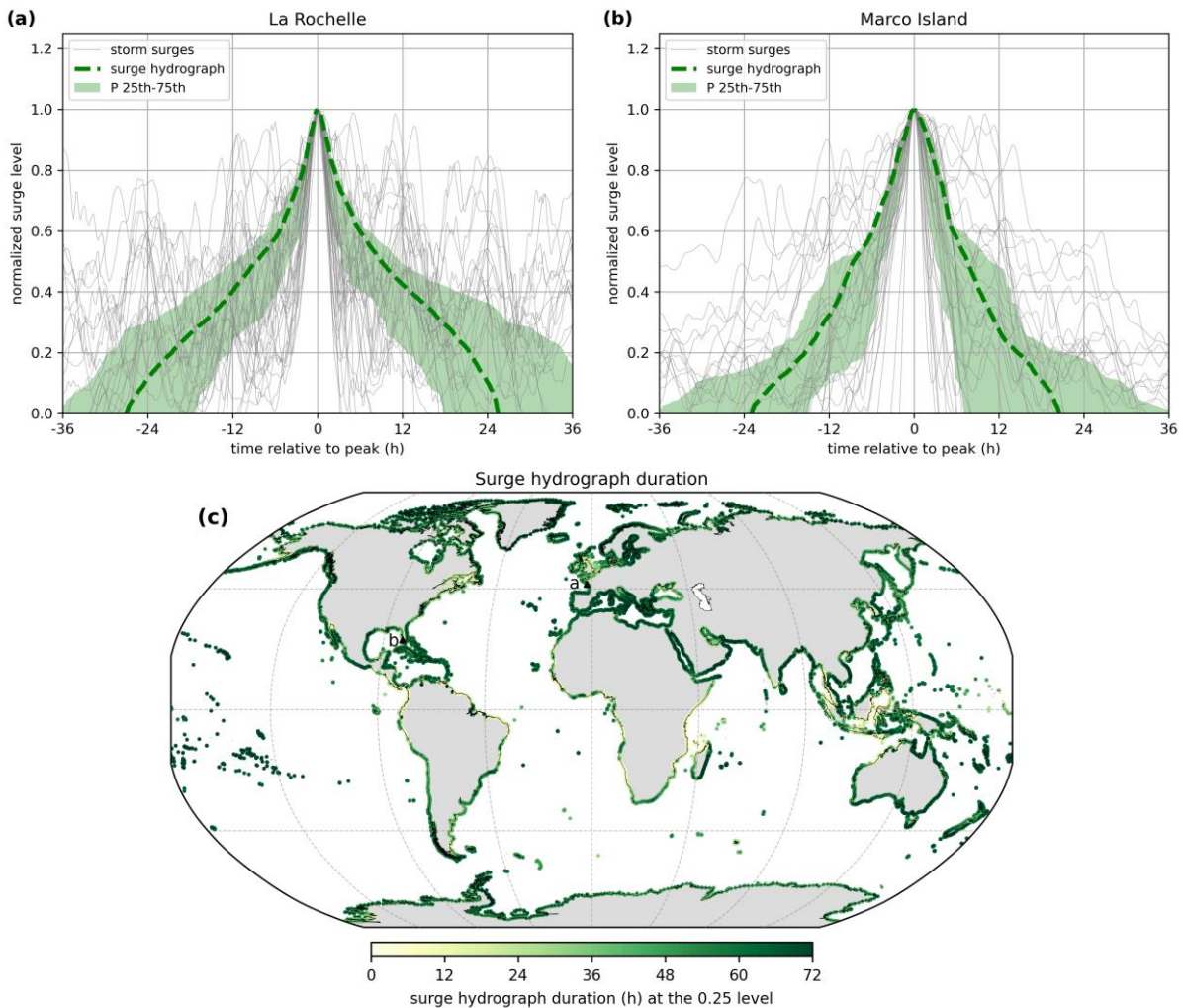
Figure 4: Surge hydrograph (dashed green line) for a) La Rochelle and b) Marco Island. Normalized surge levels are shown in grey and the green shaded area represents the 25th − 75th percentile. Panel c) shows the surge hydrograph duration at 0.25, with the locations of La Rochelle and Marco Island indicated by a and b, respectively.

299 partly explains the irregular behaviour. Differences in the evolution of storms over time can also
300 contribute to the variability observed at the different time steps of the normalized surge levels,
301 particularly in areas that are affected by TCs and ETCs as the characteristics of the two types of storms
302 differ considerably (Domingues et al., 2019). In addition, not all 40 events are extreme over their
303 complete lifetime, which means that noise is affecting the lower ends of the hydrograph. Taking the
304 mean over the normalized surge heights removes this irregular shape. At the global scale a distinct
305 pattern shows up in certain regions (*Fig. 4c*). In Europe for example, the average storm surge duration
306 is substantially lower in the North Sea compared to the Atlantic coastline and the Baltic Sea.

307 ## 4.2 Average (spring) tide signal

308 For each output location the average and spring tide signal are computed. Although the tidal range at
309 La Rochelle is substantially larger than at Marco Island, the general shape of the average tide signal is
310 comparable (*Fig. 5a & 5b*). Both locations show a large variation in amplitude between tidal cycles.
311 For spring tide, the variation in the tidal amplitude between the tidal cycles is smaller. Note that the
312 grey shaded area exceeds the red shaded area at both locations during the first and third high tide
313 because the average spring tide signal is computed by taking the average over a two week period,
314 while the average tide signal is computed by taking the average over the daily tidal cycle of 24 hours
315 and 50 minutes. Furthermore, the duration of the first and second high and low tide cycle of a tidal
316 day differs at Marco Island. This is caused by the type of tide at this location which is a mixed
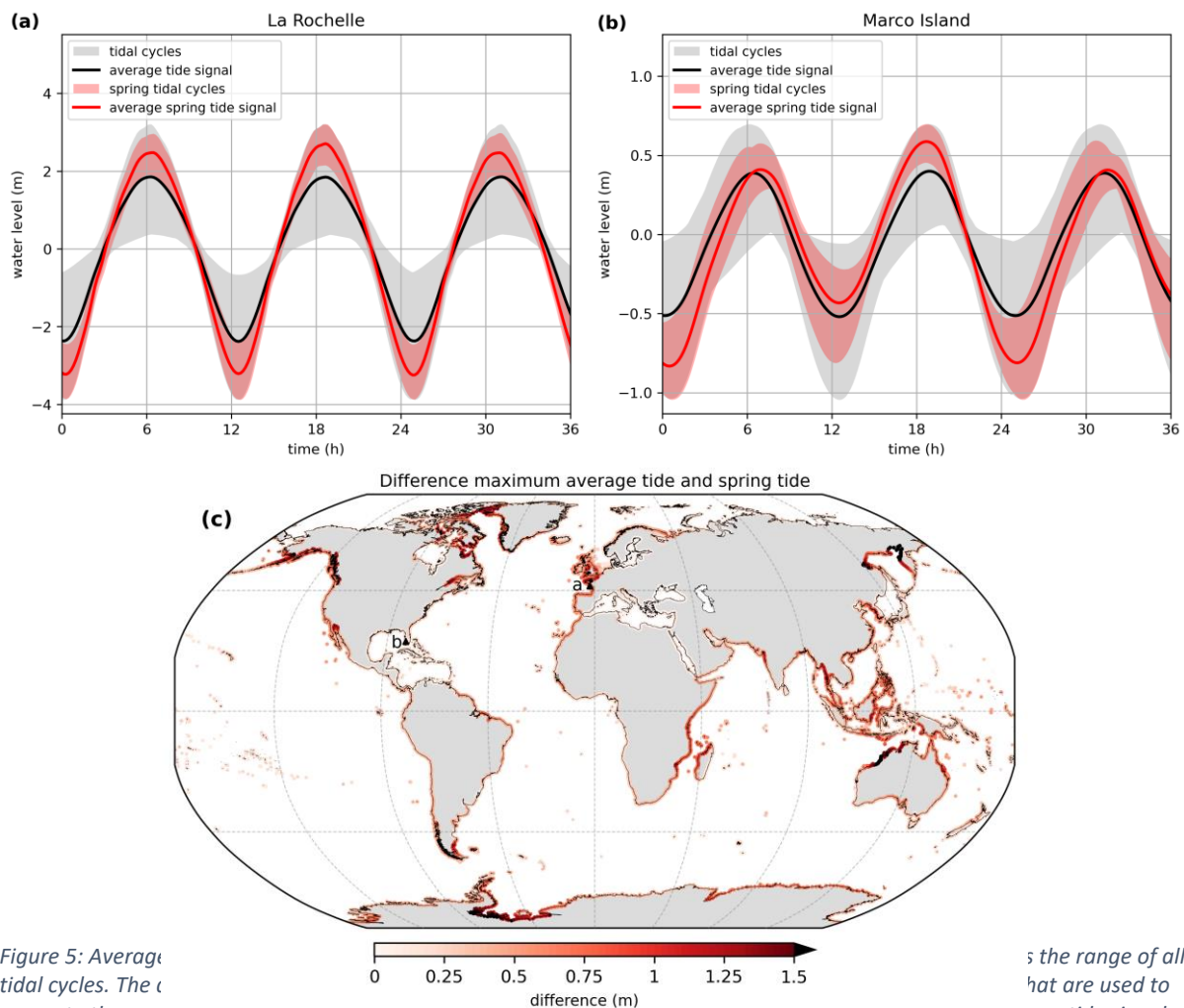
Figure 5: Average ... *s the range of all tidal cycles. The* ... *hat are used to compute the ave* ... *age tide signal and average spring tide signal. The location of La Rochelle and Marco Island are indicated by the letters a and b, respectively.*

317 semidiurnal tide (i.e. a tidal regime with two high and low tides per tidal day of different size) (Song
318 et al., 2011). Computing the average tide signal can be difficult at locations with a very small tidal
319 amplitude and mixed semidiurnal tide such a Montevideo (*Fig. A1*). Because of the large number of
320 shapes that the tidal cycles can have here, taking the average will not completely represent all possible
321 shapes. However, because the average high tide values are correctly represented by the average
322 (spring) tide signal, the findings are not affected to a large extent. For La Rochelle the maximum
323 average tide signal increases 46% from 1.85 m based on all tidal cycles to 2.70 m when taking the
324 average of the spring tidal cycles. In Marco Island the maximum average tide signal is 0.40 m and the
325 maximum average spring tide is 0.59 m (+48%). The larger absolute difference in La Rochelle means
326 that for an extreme storm tide to occur the timing of the surge maximum relative to the (spring) tide
327 maximum is more important compared to Marco Island. When applying HGRAPHER, it is important to
328 understand the typical characteristics of a storm tide in the area of interest, because this information
329 is needed to choose between the average and spring tide signal. For example, in northwest Australia
330 the difference between the maximum average and spring tide signal exceeds 1.5 m (*Fig. 5c*), indicating
331 that in this region an extreme storm tide is much more likely to occur during spring tide. Therefore,
332 using the average spring tide signal should be considered. At the global scale, the difference between
333 the average and spring tide signal maxima exceeds 0.5 m and 1.0 m, at 24% and 3% of all output
334 locations, respectively.

4.3 Storm tide hydrographs

The surge hydrograph is scaled up to a certain water level and combined with the average tide signal to obtain the storm tide hydrograph (*Fig. 6a and 6b*) that corresponds to the 1-in-100 year (RP100) storm tide level from the COAST-RP dataset (Dullaart et al., 2021b). In La Rochelle the RP100 storm tide level is 3.76 m and the average high tide is 1.85 m. Therefore, the unitless surge hydrograph is scaled up to 1.91 m, such that the combined water level equals the RP100 storm tide level. At Marco Island the RP100 storm tide level is 2.18 m to which the tide contributes 0.40 meter and the surge 1.78 meter, respectively. From the RP100 storm tide hydrograph that we create globally it is possible to deduce the relative contribution of the surge (*Fig. 6c*). Especially in areas where the maximum spring tide signal substantially exceeds (>0.5 m) the maximum average tide signal the surge contribution might be too large compared to observed historical events. This effect is counteracted by the assumption that the surge and tide coincide in time. As a result, a smaller surge is sufficient to get to the desired RP100 storm tide level compared to the situation where a time offset is implemented to combine the average tide signal with the scaled surge hydrograph. Last, the surge hydrographs are based on the surge residual including tide-surge interaction effects. These interaction effects tend to be positive at low tide and negative at high tide (Horsburgh and Wilson, 2007). As a result, we might overestimate the contribution of the surge to the combined hydrograph at high tide.
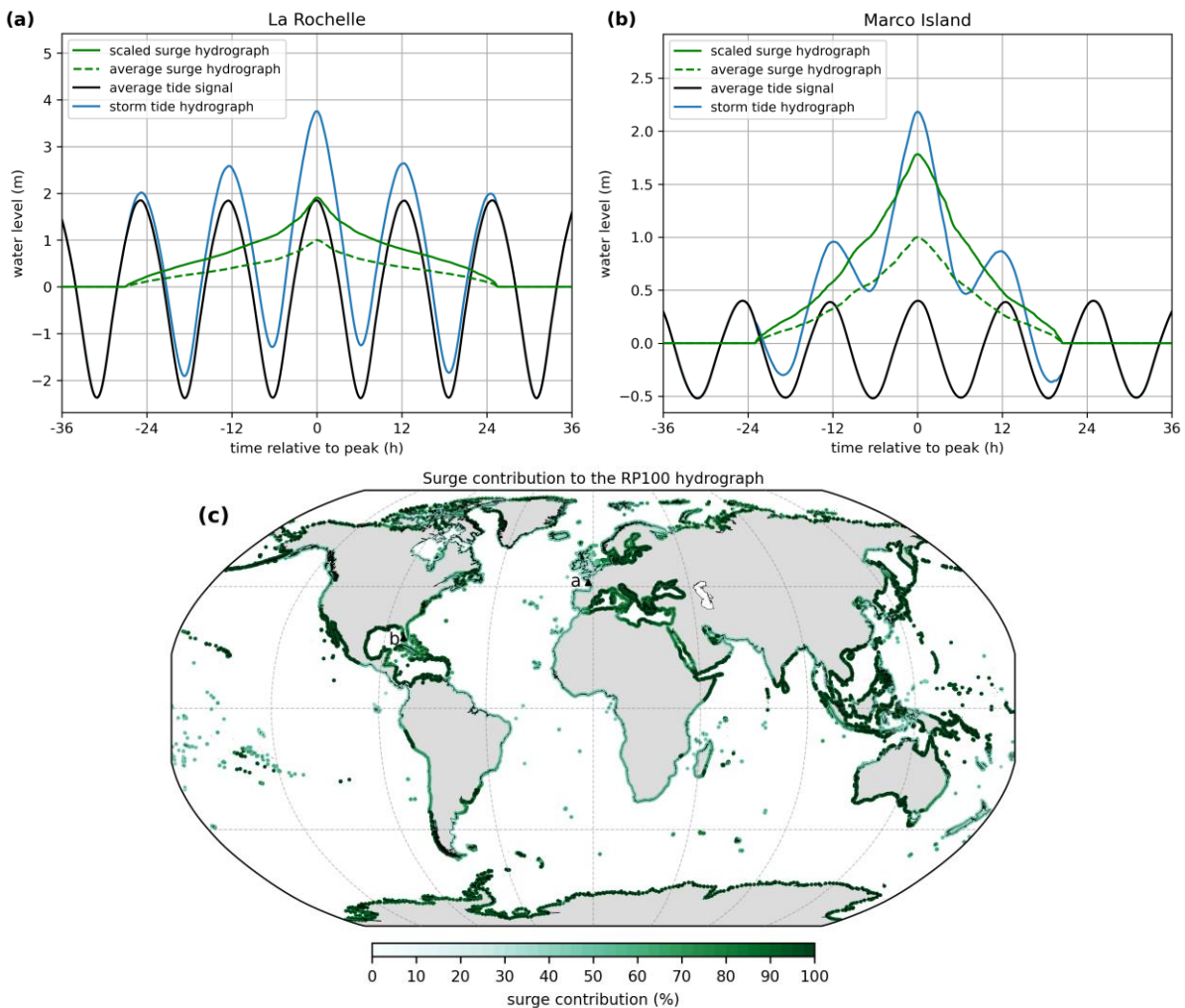
Figure 6: RP100 storm tide hydrograph (blue line) for a) La Rochelle and b) Marco Island. The average tide signal (black line), average surge hydrograph (green line), and scaled surge hydrograph (dashed green line) are also shown. Panel c) shows the relative contribution of the surge to the RP100 storm tide hydrograph maximum as a percentage. The locations of La Rochelle and Marco Island are indicated by the letters a and b, respectively.

352   4.4 Assumptions underlying the hydrograph

353   HGRAPHER is based on certain assumptions to create the storm tide hydrographs. Here, we aim to
354   better understand how these assumptions influence the results. First, we assume that the POT99
355   threshold results in the selection of a set of surge events from the residual time series that represents
356   the typical evolution of a surge event at any location. However, using a higher or lower POT percentile
357   to select surge events will give different results, depending on the typical characteristics of a location.
358   We illustrate this using La Rochelle and Marco Island as an example. Using a higher (POT99.5) or lower
359   (POT98) POT percentile does not result in a clearly deviating surge hydrograph at La Rochelle (*Fig. 7*).
360   At Marco Island however, a clear difference can be observe d between the surge hydrographs. Using
361   the higher POT99.5 percentile (i.e. only using the ~20 most extreme surge events) results in a
362   hydrograph that is more narrow and has a shorter duration. This is most likely caused by the different
363   types of storms that occur at Marco Island. Using a higher POT percentile as threshold will result in an
364   event set with a relatively larger share of TCs, compared to ETCs. This indicates that surge events
365   caused by TCs are typically shorter compared to ETC-related surge events at Marco Island. (Wahl et
366   al., (2011) also showed that the peak of the surge hydrograph can show a dependency to the intensity
367   of the underlying surge events. Overall, to select the best POT percentile to generate the surge
368   hydrograph, knowledge about the local conditions is required. For example, if surge events happen
369   very infrequently (i.e. less than once per year) a percentile higher than POT99 should be used.
370   Correspondingly, in areas where TCs occur such a higher POT percentile should be chosen if the
371   research focusses on TCs. For this, knowledge about the number of historical TC storm surge events is
372   required. Conversely, if the goal is to create a RP1 storm tide hydrograph a lower POT percentile is
373   warranted compared to when one is interested in the RP100 storm tide hydrograph.
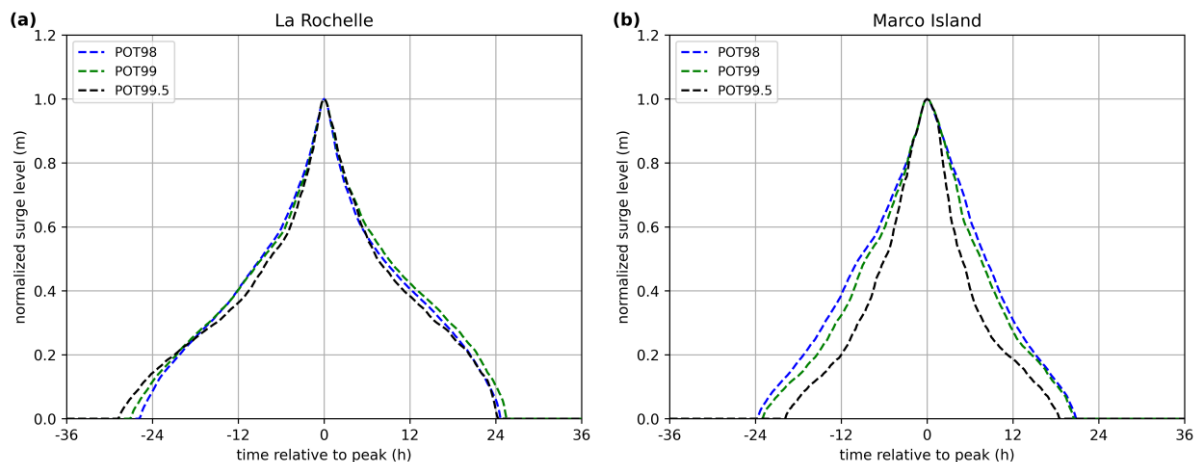
Figure 7: POT99 surge hydrograph (dashed green line) for a) La Rochelle and b) Marco Island. The blue and black dotted lines show the average surge hydrograph based on the surge events that exceed the POT98 and POT99.5 percentile.

374   Second, when combining the surge hydrograph with the average tide signal we assume that the
375   maxima of the two coincide in time. Including a time offset will lead to a storm tide hydrograph of
376   which the water level is elevated over a longer period of time, potentially increasing the severity of a
377   flood event. To test this assumption we compute the time offset at La Rochelle and Marco Island (*Fig.
378   8a & 8b*), which is defined as the timing of the maximum storm tide relative to astronomical high tide
379   (*Fig. 1*). What can be observed at both output locations is that the distribution is centred around zero.
380   However, at Marco Island the distribution is more spread out, indicated by a standard deviation of
381   0.68 compared to 0.13 for La Rochelle. At the global scale, large mean absolute time offsets are
382   observed in areas with either a very small tidal range, such as the Baltic Sea and the Mediterranean
383   Sea, or a diurnal tide regime in combination with large TC induced storm surges, such as the Gulf of

384   Mexico (*Fig. 8c*). We show the absolute time offset instead of the actual values because this way all
385   areas where large time offsets occur are revealed, including areas with both positive and negative
386   time offsets. The globally averaged absolute mean offset is 33 minutes, and the median is 9 minutes.
387   To conclude, the assumption that the surge and tide maxima coincide is appropriate at most output
388   locations. However, at certain locations it should be considered to include a time offset when creating
389   a storm tide hydrograph.
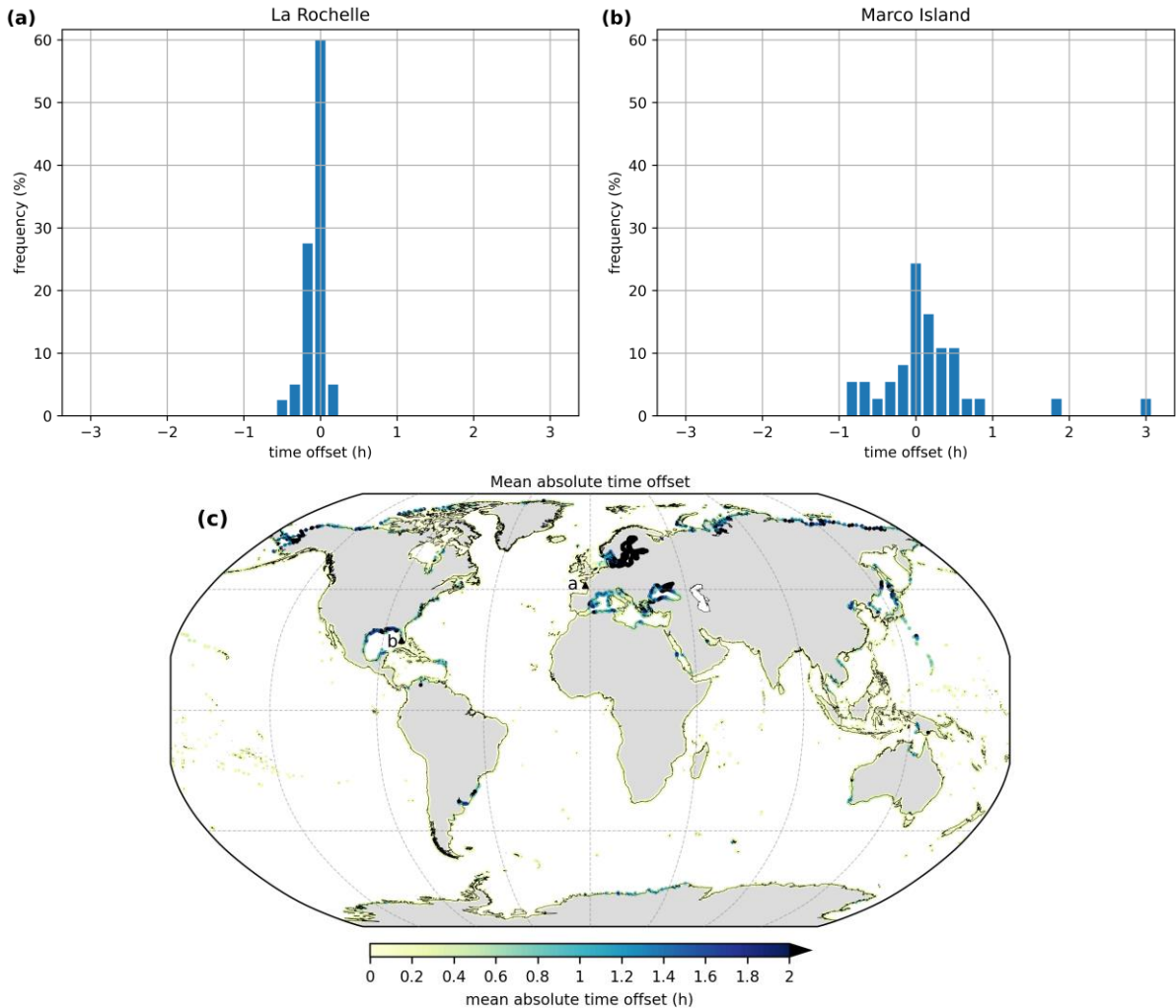
Figure 8: time offset distribution of the POT99 storm tide maxima relative to astronomical high tide at a) La Rochelle and b) Marco Island. Each blue bar represents a 10-minute period. Panel c) shows the mean absolute time offset in hours. The locations of La Rochelle and Marco Island are indicated by the letters a and b, respectively.

5 Discussion and conclusion

This study improves the ~~global~~ understanding of the duration and shape of extreme sea level events along the global coastline. It provides a novel global dataset of storm tide hydrographs which is an important first step in moving away from the planar approach towards ~~more~~ dynamic inundation modelling ~~at large scales~~. The open-source HGRAPHER model ~~that we developed that~~ can generate hydrographs ~~is called HGRAPHER~~ and allows users to create storm tide hydrographs for a RP of interest. Here, we used time series of surge, tide and storm tide levels from the CoDEC dataset (Muis et al., 2020) as input, and generated storm tide hydrographs with a 1-in-100 year return period based on COAST-RP (Dullaart et al., 2021b). Users have multiple options including, 1) use the average tide signal or spring tide signal; 2) define a POT percentile to select surge events for generating the surge hydrograph; 3) include a time offset for combining the surge hydrograph with the tide; 4) define for which RP a storm tide hydrograph should be generated; and 5) use other time series or return periods as ~~forcing~~ input data for HGRAPHER.

Several aspects of our methodology could be further improved. First, we use 38-year of surge level time series that are obtained by subtracting tidal level time series from the storm tide level. As a result, the surge time series do not only contain the meteorological contribution to the sea level, but also contain tide-surge interaction effects~~, generally referred to as the residual water level~~ (Horsburgh and Wilson, 2007). This could be addressed by using a 'surge-only' simulation, which would not be affected by interaction effects. Another aspect that could be improved is that our analysis is based on a ~~40~~ 38 years timeseries. This provides a limited number of events, specifically for regions that do not regularly experience extremes such as the ~~Caribbean~~equatorial regions. Potentially we could extend our analysis by using a large set of synthetic events, such as those presented for TCs in (Dullaart et al., 2021a). For extra-tropical regions, seasonal forecasts could be used to create a large ensemble of events (Haarsma et al., 2016). The advantage of a large set~~r sample~~ of synthetic events is that it would allow to assess if hydrographs are different for different RPs. This is currently not possible because of the small sample size.

Second, we do not account for different types of storms. TCs and ETCs have distinct meteorological characteristics resulting in a different evolution of the water level over time. For example, TCs can have stronger wind speeds and lower air pressure than ETCs, resulting in a higher storm surge (Keller and DeVecchio, 2016). ETCs on the other hand generally affect a larger coastal area because they are often larger in size than TCs (Irish et al., 2008). The typical radius of a TC is between 100 and 500 km while for an ETC it is in the range of 100-2000 km. In addition, once TCs move inland the wind direction can become offshore directly at the coast, resulting in a storm surge sign that quickly changes from positive to negative. An example of this is during TC Irma, which made landfall in Florida in 2017 (Cheng and Wang, 2019). A potential direction for future research would be to separate storm surges by type of storm that caused them and develop a surge hydrograph individually for TCs and ETCs. This would require much longer surge time-series (representing thousands of years instead of decades) that could be created using, for example, large climate model ensembles (Haarsma et al., 2016) or synthetic tracks of TCs (Bloemendaal et al., 2020).

Third, the average tide signal is computed by taking the average over thousands of tidal cycles with a duration of 1 lunar day, lasting 24 hours and 50 minutes. For the majority of the output locations HGRAPHER correctly extracts the average (spring) tide signal. However, in areas with a mixed tidal regime the daily uneven magnitude of the two high tides are averaged out. This is because over time it alters whether the first or second high tide is the highest tide during that lunar day. Including the mixed tidal regime characteristics at these locations, such as Montevideo (*App. A*), would result in a

435 more realistic storm tide hydrograph. However, for this multiple storm tide hydrographs have to be
436 generated ~~that can be applied to different RPs~~that have different shapes but reach the same maximum
437 water level. This would makes the storm tide hydrographs dataset less easily applicabley to implement
438 in large scale flood hazard assessments.

439 A final limitation is that our analysis does not include waves. Wave setup can increase storm tide levels
440 at the coast. Therefore, it is often an important component of extreme sea levels, and including a
441 dynamic wave setup component in HGRAPHER is a potential direction for future research. To
442 accomplish this, we could make use of a parametric approach that has been used in previous global
443 scale studies to obtain estimates of wave setup (Vousdoukas et al., 2018; Kirezci et al., 2020).

444 HGRAPHER and the global dataset of storm tide hydrographs improve our understanding of the
445 duration and shape of storm tide levels. They provide a basis to move towards more dynamic
446 inundation modelling at large scales, and Aas a next step, the hydrographs could be applied as
447 boundary conditions in inundation modelling ~~and thereby provide a basis to move towards more~~
448 ~~dynamic inundation modelling at large scales. More specifically, the storm tide hydrographs can be~~
449 ~~used as boundary conditions for large scale dynamic inundation modelling~~. This way, the time
450 component is taken into account when modelling inundation which will substantially improve the
451 accuracy of large-scale coastal flood hazard assessments.

452 **6 Appendices**
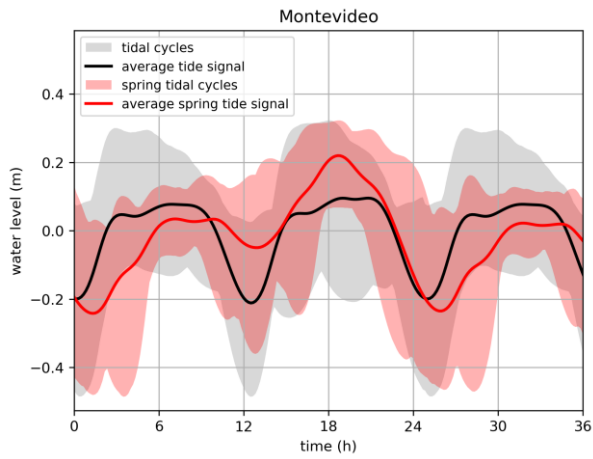
Figure A1: Average tide signal (black line) for Montevideo. The grey shaded area shows the range of all tidal cycles. The average spring tide signal is shown in red and the red shaded area indicate all tidal cycles that are used to compute the average spring tide signal.

453

7 Code availability

The HGRAPHER method developed in this study consists of several scripts that are available from GitHub at github.com/jobdullaart/HGRAPHER

8 Data availability

Sea level time series used in this study (CoDEC dataset) are available from the Copernicus Climate Data Store (CDS) at doi.org/10.24381/cds.a6d42d60. In addition, the hydrographs generated in this study are available from the 4TU data repository at doi.org/10.4121/21270948.

9 Author contribution

JD developed the HGRAPHER method and wrote the paper. SM, HM, DE, PW, and JA participated in technical discussions and co-wrote the paper.

10 Competing interests

The authors declare that they have no conflict of interest.

11 Acknowledgements

We would like to thank Nathalie van Veen for her active involvement in the interpretation of the model outcomes and her critical look at the methodology. J.D. and J.A. received funding from the COASTRISK project financed by the SCOR Corporate Foundation for Science (R/003316.01). J.A. is also funded by the ERC Advanced Grant COASTMOVE #884442. S.M. received funding from the research program MOSAIC with project number ASDI.2018.036, which is financed by the Netherlands Organization for Scientific Research (NWO). D.E. and P.W. received funding from the NWO in the form of a VIDI grant (grant no. 016.161.324). This work was sponsored by NWO Exact and Natural Sciences for the use of supercomputer facilities (grant no. 2020.007).

12 References

Bates, P. D., Horritt, M. S., and Fewtrell, T. J.: A simple inertial formulation of the shallow water equations for efficient two-dimensional flood inundation modelling, J. Hydrol., 387, 33–45, https://doi.org/10.1016/j.jhydrol.2010.03.027, 2010.

Bloemendaal, N., Muis, S., Haarsma, R. J., Verlaan, M., Irazoqui Apecechea, M., de Moel, H., Ward, P. J., and Aerts, J. C. J. H.: Global modeling of tropical cyclone storm surges using high resolution forecasts, Clim. Dyn., 52, 5031, https://doi.org/10.1007/s00382-018-4430-x, 2019.

Bloemendaal, N., Haigh, I. D., Moel, H. De, Muis, S., Haarsma, R. J., and Aerts, J. C. J. H.: Generation of a global synthetic tropical cyclone hazard dataset using STORM, Sci. Data, 7, https://doi.org/10.1038/s41597-020-0381-2, 2020.

Brown, S., Nicholls, R. J., Goodwin, P., Haigh, I. D., Lincke, D., Vafeidis, A. T., and Hinkel, J.: Quantifying Land and People Exposed to Sea-Level Rise with No Mitigation and 1.5°C and 2.0°C Rise in Global Temperatures to Year 2300, Earth's Futur., 6, 583–600, https://doi.org/10.1002/2017EF000738, 2018.

Chbab, H.: Waterstandsverlopen kust. Wettelijk Toetsinstrumentarium WTI-2017, Delft, 2015.

Cheng, J. and Wang, P.: Unusual Beach Changes Induced by Hurricane Irma with a Negative Storm Surge and Poststorm Recovery, J. Coast. Res., 35, 1185–1199, https://doi.org/10.2112/JCOASTRES-D-19-00038.1, 2019.

Colle, B. A., Rojowsky, K., and Buonaito, F.: New York city storm surges: Climatology and an analysis of the wind and cyclone evolution, J. Appl. Meteorol. Climatol., 49, 85–100, https://doi.org/10.1175/2009JAMC2189.1, 2010.

Dee, D. P., Uppala, S. M., Simmons, A. J., Berrisford, P., Poli, P., Kobayashi, S., Andrae, U., Balmaseda, M. A., Balsamo, G., Bauer, P., Bechtold, P., Beljaars, A. C. M., van de Berg, L., Bidlot, J., Bormann, N., Delsol, C., Dragani, R., Fuentes, M., Geer, A. J., Haimberger, L., Healy, S. B., Hersbach, H., Hólm, E. V., Isaksen, L., Kållberg, P., Köhler, M., Matricardi, M., Mcnally, A. P., Monge-Sanz, B. M., Morcrette, J. J., Park, B. K., Peubey, C., de Rosnay, P., Tavolato, C., Thépaut, J. N., and Vitart, F.: The ERA-Interim reanalysis: Configuration and performance of the data assimilation system, Q. J. R. Meteorol. Soc., 137, 553–597, https://doi.org/10.1002/qj.828, 2011.

Domingues, R., Kuwano-Yoshida, A., Chardon-Maldonado, P., Todd, R. E., Halliwell, G. R., Kim, H. S., Lin, I. I., Sato, K., Narazaki, T., Shay, L. K., Miles, T., Glenn, S., Zhang, J. A., Jayne, S. R., Centurioni, L. R., Le Hénaff, M., Foltz, G., Bringas, F., Ali, M. M., DiMarco, S., Hosoda, S., Fukuoka, T., LaCour, B., Mehra, A., Sanabia, E. R., Gyakum, J. R., Dong, J., Knaff, J., and Goni, G. J.: Ocean observations in support of studies and forecasts of tropical and extratropical cyclones, Front. Mar. Sci., 6, 1–23, https://doi.org/10.3389/fmars.2019.00446, 2019.

Dullaart, J. C. M., Muis, S., Bloemendaal, N., and Aerts, J. C. J. H.: Advancing global storm surge modelling using the new ERA5 climate reanalysis, Clim. Dyn., 54, 1007–1021, https://doi.org/10.1007/s00382-019-05044-0, 2020.

Dullaart, J. C. M., Muis, S., Bloemendaal, N., Chertova, M. V., Couasnon, A., and Aerts, J. C. J. H.: Accounting for tropical cyclones more than doubles the global population exposed to low-probability coastal flooding, Commun. Earth Environ., 2, 1–11, https://doi.org/10.1038/s43247-021-00204-9, 2021a.

Dullaart, J. C. M., Muis, S., Bloemendaal, N., Chertova, M., Couasnon, A., and Aerts, J. C. J. H.: COAST-RP: A global COastal dAtaset of Storm Tide Return Periods, https://doi.org/https://doi.org/10.4121/13392314, 2021b.

523 Environment Agency: Coastal flood boundary conditions for the UK: 2018 update, Bristol, 116 pp.,
524 2018.

525 FEMA: The national flood insurance act of 1968, Natl. flood Insur. act 1968, 1968.

526 Haarsma, R. J., Roberts, M. J., Vidale, P. L., Catherine, A., Bellucci, A., Bao, Q., Chang, P., Corti, S.,
527 Fučkar, N. S., Guemas, V., Von Hardenberg, J., Hazeleger, W., Kodama, C., Koenigk, T., Leung, L. R.,
528 Lu, J., Luo, J. J., Mao, J., Mizielinski, M. S., Mizuta, R., Nobre, P., Satoh, M., Scoccimarro, E., Semmler,
529 T., Small, J., and Von Storch, J. S.: High Resolution Model Intercomparison Project (HighResMIP v1.0)
530 for CMIP6, Geosci. Model Dev., 9, 4185–4208, https://doi.org/10.5194/gmd-9-4185-2016, 2016.

531 Haer, T., Botzen, W. J. W., Van Roomen, V., Connor, H., Zavala-Hidalgo, J., Eilander, D. M., and Ward,
532 P. J.: Coastal and river flood risk analyses for guiding economically optimal flood adaptation policies:
533 A country-scale study for Mexico, Philos. Trans. R. Soc. A Math. Phys. Eng. Sci., 376,
534 https://doi.org/10.1098/rsta.2017.0329, 2018.

535 Haigh, I. D., Wadey, M. P., Wahl, T., Ozsoy, O., Nicholls, R. J., Brown, J. M., Horsburgh, K., and
536 Gouldby, B.: Spatial and temporal analysis of extreme sea level and storm surge events around the
537 coastline of the UK, Sci. Data, 3, 1–14, https://doi.org/10.1038/sdata.2016.107, 2016.

538 Hersbach, H., Bell, B., Berrisford, P., Horányi, A., Munoz Sabater, J., Nicolas, J., Radu, R., Schepers, D.,
539 Simmons, A., Soci, C., and Dee, D.: Global reanalysis: goodbye ERA-Inteirm, hello ERA5, ECMWF
540 Newsl., 159, 17–24, https://doi.org/10.21957/vf291hehd7, 2019.

541 Horsburgh, K. J. and Wilson, C.: Tide-surge interaction and its role in the distribution of surge
542 residuals in the North Sea, J. Geophys. Res. Ocean., 112, https://doi.org/10.1029/2006JC004033,
543 2007.

544 Idier, D., Bertin, X., Thompson, P., and Pickering, M. D.: Interactions Between Mean Sea Level, Tide,
545 Surge, Waves and Flooding: Mechanisms and Contributions to Sea Level Variations at the Coast,
546 Surv. Geophys., 40, 1603–1630, https://doi.org/10.1007/s10712-019-09549-5, 2019.

547 Irish, J. L., Resio, D. T., and Ratcliff, J. J.: The Influence of Storm Size on Hurricane Surge, J. Phys.
548 Oceanogr., 38, 2003–2013, https://doi.org/10.1175/2008JPO3727.1, 2008.

549 Keller, E. A. and DeVecchio, D. E.: Hurricanes and Extratropical Cyclones, in: Natural Hazards: Earth's
550 Processes as Hazards, Disasters, and Catastrophes, Routledge, New York, 331–363, 2016.

551 Kirezci, E., Young, I. R., Ranasinghe, R., Muis, S., Nicholls, R. J., Lincke, D., and Hinkel, J.: Projections of
552 global-scale extreme sea levels and resulting episodic coastal flooding over the 21st century, Sci.
553 Rep., 10, https://doi.org/10.1038/s41598-020-67736-6, 2020.

554 Lamb, R., Brisley, R., Hunter, N., Wingfield, S., Warren, S., Mattingley, P., and Sayers, P.: Flood
555 Standards of Protection and Risk Management Activities Final Report JBA Project Manager, North
556 Yorkshire, 74 pp., 2018.

557 Leijnse, T., van Ormondt, M., Nederhoff, K., and van Dongeren, A.: Modeling compound flooding in
558 coastal systems using a computationally efficient reduced-physics solver: Including fluvial, pluvial,
559 tidal, wind- and wave-driven processes, Coast. Eng., 163, 103796,
560 https://doi.org/10.1016/j.coastaleng.2020.103796, 2021.

561 Lewis, M., Bates, P., Horsburgh, K., Neal, J., and Schumann, G.: A storm surge inundation model of
562 the northern Bay of Bengal using publicly available data, Q. J. R. Meteorol. Soc., 139, 358–369,
563 https://doi.org/10.1002/qj.2040, 2013.

564 Lincke, D. and Hinkel, J.: Economically robust protection against 21st century sea-level rise, Glob.
565 Environ. Chang., 51, 67–73, https://doi.org/10.1016/j.gloenvcha.2018.05.003, 2018.

566 MacPherson, L. R., Arns, A., Dangendorf, S., Vafeidis, A. T., and Jensen, J.: A Stochastic Extreme Sea
567 Level Model for the German Baltic Sea Coast, J. Geophys. Res. Ocean., 124, 2054–2071,
568 https://doi.org/10.1029/2018JC014718, 2019.

569 Merkens, J. L., Reimann, L., Hinkel, J., and Vafeidis, A. T.: Gridded population projections for the
570 coastal zone under the Shared Socioeconomic Pathways, Glob. Planet. Change, 145, 57–66,
571 https://doi.org/10.1016/j.gloplacha.2016.08.009, 2016.

572 Muis, S., Verlaan, M., Winsemius, H. C., Aerts, J. C. J. H., and Ward, P. J.: A global reanalysis of storm
573 surges and extreme sea levels, Nat. Commun., 7, https://doi.org/10.1038/ncomms11969, 2016.

574 Muis, S., Apecechea, M. I., Dullaart, J., de Lima Rego, J., Madsen, K. S., Su, J., Yan, K., and Verlaan, M.:
575 A High-Resolution Global Dataset of Extreme Sea Levels, Tides, and Storm Surges, Including Future
576 Projections, Front. Mar. Sci., 7, https://doi.org/10.3389/fmars.2020.00263, 2020.

577 Oppenheimer, M., Glavovic, B. C., Hinkel, J., van de Wal, R., Magnan, A. K., Abd-Elgawad, A., Cai, R.,
578 Cifuentes-Jara, M., DeConto, R. M., Ghosh, T., Hay, J., Isla, F., Marzeion, B., Meyssignac, B., and
579 Sebesvari, Z.: Sea level rise and implications for low lying islands, coasts and communities, edited by:
580 Pörtner, H. O., Roberts, D. C., Masson-Delmotte, V., Zhai, P., Tignor, M., Poloczanska, E., Mintenbeck,
581 K., Alegría, A., Nicolai, M., Okem, A., Petzold, J., Rama, B., and Weyer, N. M., 2019.

582 Pasquier, U., He, Y., Hooton, S., Goulden, M., and Hiscock, K. M.: An integrated 1D–2D hydraulic
583 modelling approach to assess the sensitivity of a coastal region to compound flooding hazard under
584 climate change, Nat. Hazards, 98, 915–937, https://doi.org/10.1007/s11069-018-3462-1, 2019.

585 Pugh, D. T.: Tides, Surges and mean sea-level (Reprinted with corrections), John Wiley & Sons, Ltd.,
586 Chichester, U.K, 486 pp., https://doi.org/10.1016/0264-8172(88)90013-X, 1996.

587 Quinn, N., Lewis, M., Wadey, M. P., and Haigh, I. D.: Assessing the temporal variability in extreme
588 storm-tide time series for coastal flood risk assessment, J. Geophys. Res. Ocean., 119, 4983–4998,
589 https://doi.org/10.1002/2014JC010197, 2014.

590 Ramirez, J. A., Lichter, M., Coulthard, T. J., and Skinner, C.: Hyper-resolution mapping of regional
591 storm surge and tide flooding: comparison of static and dynamic models, Nat. Hazards, 82, 571–590,
592 https://doi.org/10.1007/s11069-016-2198-z, 2016.

593 Rego, J. L. and Li, C.: Nonlinear terms in storm surge predictions: Effect of tide and shelf geometry
594 with case study from Hurricane Rita, J. Geophys. Res. Ocean., 115, 1–19,
595 https://doi.org/10.1029/2009JC005285, 2010.

596 Resio, D. T. and Westerink, J. J.: Modeling the physics of storm surges, Phys. Today, 61, 33–38, 2008.

597 Salisbury, M. B. and Hagen, S. C.: The effect of tidal inlets on open coast storm surge hydrographs,
598 Coast. Eng., 54, 377–391, https://doi.org/10.1016/j.coastaleng.2006.10.002, 2007.

599 Santamaria-Aguilar, S. and Vafeidis, A. T.: Are Extreme Skew Surges Independent of High Water
600 Levels in a Mixed Semidiurnal Tidal Regime?, J. Geophys. Res. Ocean., 123, 8877–8886,
601 https://doi.org/10.1029/2018JC014282, 2018.

602 Santamaria-Aguilar, S., Arns, A., and Vafeidis, A. T.: Sea-level rise impacts on the temporal and
603 spatial variability of extreme water levels: A case study for St. Peter-Ording, Germany, J. Geophys.
604 Res. Ocean., 122, 2742–2759, https://doi.org/10.1002/2016JC012579, 2017.

605 Sebastian, A., Proft, J., Dietrich, J. C., Du, W., Bedient, P. B., and Dawson, C. N.: Characterizing
606 hurricane storm surge behavior in Galveston Bay using the SWAN+ADCIRC model, Coast. Eng., 88,
607 171–181, https://doi.org/10.1016/j.coastaleng.2014.03.002, 2014.

608 Song, D., Wang, X. H., Kiss, A. E., and Bao, X.: The contribution to tidal asymmetry by different

609   combinations of tidal constituents, J. Geophys. Res. Ocean., 116, 1–12,
610   https://doi.org/10.1029/2011JC007270, 2011.

611   Stephens, S. A., Paulik, R., Reeve, G., Wadhwa, S., Popovich, B., Shand, T., and Haughey, R.: Future
612   changes in built environment risk to coastal flooding, permanent inundation and coastal erosion
613   hazards, J. Mar. Sci. Eng., 9, https://doi.org/10.3390/jmse9091011, 2021.

614   Tiggeloven, T., De Moel, H., Winsemius, H. C., Eilander, D., Erkens, G., Gebremedhin, E., Diaz Loaiza,
615   A., Kuzma, S., Luo, T., Iceland, C., Bouwman, A., Van Huijstee, J., Ligtvoet, W., and Ward, P. J.: Global-
616   scale benefit-cost analysis of coastal flood adaptation to different flood risk drivers using structural
617   measures, Nat. Hazards Earth Syst. Sci., 20, 1025–1044, https://doi.org/10.5194/nhess-20-1025-
618   2020, 2020.

619   Vafeidis, A. T., Schuerch, M., Wolff, C., Spencer, T., Merkens, J. L., Hinkel, J., Lincke, D., Brown, S., and
620   Nicholls, R. J.: Water-level attenuation in broad-scale assessments of exposure to coastal flooding: a
621   sensitivity analysis, Nat. Hazards Earth Syst. Sci., 19, 973–984, https://doi.org/10.5194/nhess-2018-
622   359, 2019.

623   Vousdoukas, M. I., Voukouvalas, E., Mentaschi, L., Dottori, F., Giardino, A., Bouziotas, D., Bianchi, A.,
624   Salamon, P., and Feyen, L.: Developments in large-scale coastal flood hazard mapping, Nat. Hazards
625   Earth Syst. Sci., 16, 1841–1853, https://doi.org/10.5194/nhess-16-1841-2016, 2016a.

626   Vousdoukas, M. I., Voukouvalas, E., Annunziato, A., Giardino, A., and Feyen, L.: Projections of
627   extreme storm surge levels along Europe, Clim. Dyn., 47, 1–20, https://doi.org/10.1007/s00382-016-
628   3019-5, 2016b.

629   Vousdoukas, M. I., Mentaschi, L., Voukouvalas, E., Verlaan, M., Jevrejeva, S., Jackson, L. P., and
630   Feyen, L.: Global probabilistic projections of extreme sea levels show intensification of coastal flood
631   hazard, Nat. Commun., 9, 2360, https://doi.org/10.1038/s41467-018-04692-w, 2018.

632   Wahl, T., Mudersbach, C., and Jensen, J.: Assessing the hydrodynamic boundary conditions for risk
633   analyses in coastal areas: A stochastic storm surge model, Nat. Hazards Earth Syst. Sci., 11, 2925–
634   2939, https://doi.org/10.5194/nhess-11-2925-2011, 2011.

635   Wahl, T., Mudersbach, C., and Jensen, J.: Assessing the hydrodynamic boundary conditions for risk
636   analyses in coastal areas: A multivariate statistical approach based on Copula functions, Nat. Hazards
637   Earth Syst. Sci., 12, 495–510, https://doi.org/10.5194/nhess-12-495-2012, 2012.

638   Wahl, T., Haigh, I. D., Nicholls, R. J., Arns, A., Dangendorf, S., Hinkel, J., and Slangen, A. B. A.:
639   Understanding extreme sea levels for broad-scale coastal impact and adaptation analysis, Nat.
640   Commun., 8, 1–12, https://doi.org/10.1038/ncomms16075, 2017.

641   Ward, P. J., Jongman, B., Salamon, P., Simpson, A., Bates, P., De Groeve, T., Muis, S., De Perez, E. C.,
642   Rudari, R., Trigg, M. A., and Winsemius, H. C.: Usefulness and limitations of global flood risk models,
643   Nat. Clim. Chang., 5, 712–715, https://doi.org/10.1038/nclimate2742, 2015.

644   Williams, J., Horsburgh, K. J., Williams, J. A., and Proctor, R. N. F.: Tide and skew surge independence:
645   New insights for flood risk, Geophys. Res. Lett., 43, 6410–6417,
646   https://doi.org/10.1002/2016GL069522, 2016.

647   Xu, S. and Huang, W.: An improved empirical equation for storm surge hydrographs in the Gulf of
648   Mexico, U.S.A, Ocean Eng., 75, 174–179, https://doi.org/10.1016/j.oceaneng.2013.11.004, 2014.

649   Yin, J., Lin, N., and Yu, D.: Coupled modeling of storm surge and coastal inundation: A case study in
650   New York City during Hurricane Sandy, Water Resour. Res., 52, 8685–8699,
651   https://doi.org/10.1002/2016WR019102, 2016.

652